Geotechnical Aspects of the 2015 M_w 8.3 Illapel Megathrust Earthquake Sequence in Chile

Gabriel Candia,[a),e)] Gregory P. de Pascale,[b),g)] Gonzalo Montalva,[c),f)] and Christian Ledezma[d),e)]

The 2015 Illapel earthquake sequence in Central Chile, occurred along the subduction zone interface in a known seismic gap, with moment magnitudes of M_w 8.3, M_w 7.1, and M_w 7.6. The main event triggered tsunami waves that damaged structures along the coast, while the surface ground motion induced localized liquefaction, settlement of bridge abutments, rockfall, debris flow, and collapse in several adobe structures. Because of the strict seismic codes in Chile, damage to modern engineered infrastructure was limited, although there was widespread tsunami-induced damage to one-story and two-stories residential homes adjacent to the shoreline. Soon after the earthquake, shear wave measurements were performed at selected potentially liquefiable sites to test recent V_S-based liquefaction susceptibility approaches. This paper describes the effects that this earthquake sequence and tsunami had on a number of retaining structures, bridge abutments, and cuts along Chile's main highway (Route 5). Since tsunami waves redistribute coastal and near shore sand along the coast, liquefaction evidence in coastal zones with tsunami waves is sometimes obscured within minutes because the tsunami waves entrain and deposit sand that covers or erodes evidence of liquefaction (e.g., lateral spread or sand blows). This suggests that liquefaction occurrence and hazard may be under estimated in coastal zones. Importantly, the areas that experienced the greatest coseismic slip, appeared to have the largest volumes of rockfall that impacted roads, which suggests that coseismic slip maps, generated immediately after the shaking stops, can provide a first order indication about where to expect damage during future major events. [DOI: 10.1193/031716EQS043M]

[a)] Facultad de Ingeniería Civil, Universidad del Desarrollo, Av. Plaza 680 Las Condes, Santiago, Chile
[b)] Departamento de Geología y Facultad de Ciencias Físicas y Matemáticas (FCFM), Universidad de Chile, Plaza Ercilla 803, Santiago, Chile
[c)] Departamento de Ingeniería Civil, Universidad de Concepción, Edmundo Larenas 215 Barrio Universitario Concepción
[d)] Pontificia Universidad Católica de Chile, Vicuña Mackenna 4860, Macul, Santiago, Chile
[e)] National Research Center for Integrated Natural Disaster Management, CIGIDEN, CONICYT/FONDAP/15110017
[f)] Water Research Center for Agriculture and Mining, CRHIAM, CONICYT/FONDAP/15130015
[g)] Centro de Excelencia en Geotermia de Los Andes (CEGA), CEGA FONDAP CONICYT 15090013

INTRODUCTION

A megathrust subduction earthquake affected central Chile on 16 September 2015 (22:54:32 UTC), approximately 50 km west of Illapel (Figure 1). The Chilean National Seismological Center (CSN) estimated the magnitude (M_w) in 8.4 and located the hypocenter at 31.637° south latitude and 71.741° west longitude at a depth of 23.3 km. The U.S. Geological Survey (USGS) estimated the magnitude (M_w) in 8.3, and located the hypocenter at 31.573° south latitude and 71.674° west longitude at a depth of 22.4 km. According to USGS, the rupture plane strikes 353° and dips west to east at about 19° (USGS 2016). The earthquake ruptured a 230 km × 100 km section of the boundary between the Nazca Plate and the South American plate (Tilmann et al. 2016), which has an average convergence rate of 68–80 mm/yr (Dura et al. 2015). A maximum slip of 5–6 m along the plate interface was modelled using displacement measurements and seismic waveforms (Tilmann et al. 2016). The main event was immediately followed by tsunami waves with a maximum run-up height of 11 m above sea level measured just north of the epicenter (GEER 2015, Aránguiz 2016) and several aftershocks, including a M_w 7.1 (22:59:15 UTC) and a M_w 7.6 (23:18:35 UTC) earthquake. The earthquakes and tsunami effects were observed from Valparaiso (180 km south of the hypocenter) to La Serena (190 km north of the hypocenter), and the ground shaking was felt as far as Buenos Aires, Uruguay, and Southern Brazil, locations over 1,200 km east of the epicenter and within stable continental regions.

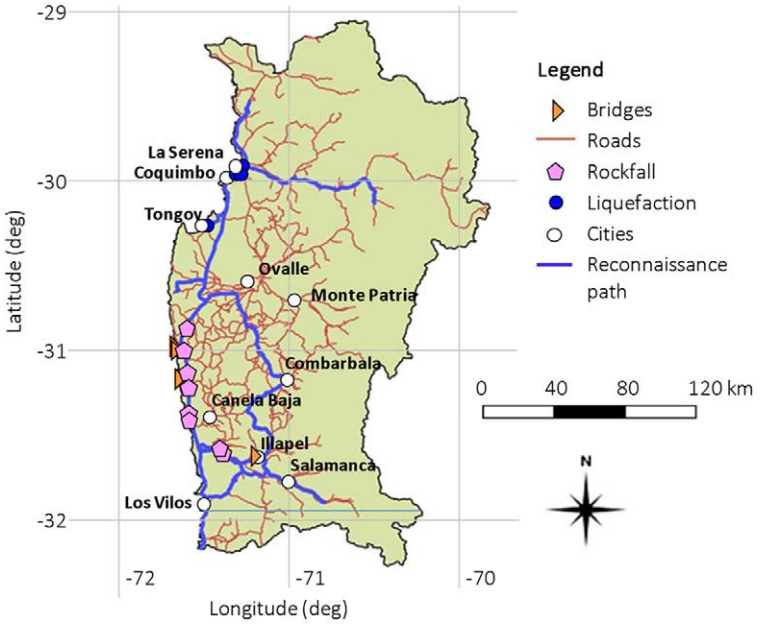

Figure 1. Schematic view of the Coquimbo Region in Central Chile, visited sites and reconnaissance path.

The 2015 Illapel earthquake is part of a series of megathrust earthquakes with moment magnitudes greater than 8.0, which struck Central Chile over the past three hundred years. Recent studies (e.g., Dura et al. 2015 and references within) suggest that the area is due for a magnitude 9.0 earthquake or greater, or similar to the M_w 8.7 Valparaíso earthquake of 1730. Therefore, understanding and documenting the impact of a smaller event, such as the 2015 M_w 8.3 Illapel earthquake, is key for planning and anticipating the effects of a much larger one. The 2015 earthquake filled a large seismic zone between the 1985 Valparaiso earthquake (M_w 7.9) and the 1922 Vallenar earthquake (M_w 8.7), as shown in Figure 2. The gap previously ruptured during the 1943 Ovalle (M_w 7.9) and during the great 1730 Valparaiso (M_w 8.7) events.

A group of researchers from CIGIDEN (Universidad Católica), CRHIAM (Universidad de Concepción), and Universidad de Chile (UChile) conducted field reconnaissance to document the geotechnical effects of the earthquake and tsunami. Despite the large magnitude of the main event and aftershocks, the overall impact from ground motions on the infrastructure was limited. The reconnaissance team focused on the cities of Coquimbo and La Serena, where ground failure and flooding caused severe damage to the coastline, completely shutting down the port, interrupting vital lifelines, and triggering liquefaction within deposits adjacent to the coast. Researchers identified several cases of rockfall, damage to mitigation fences, and

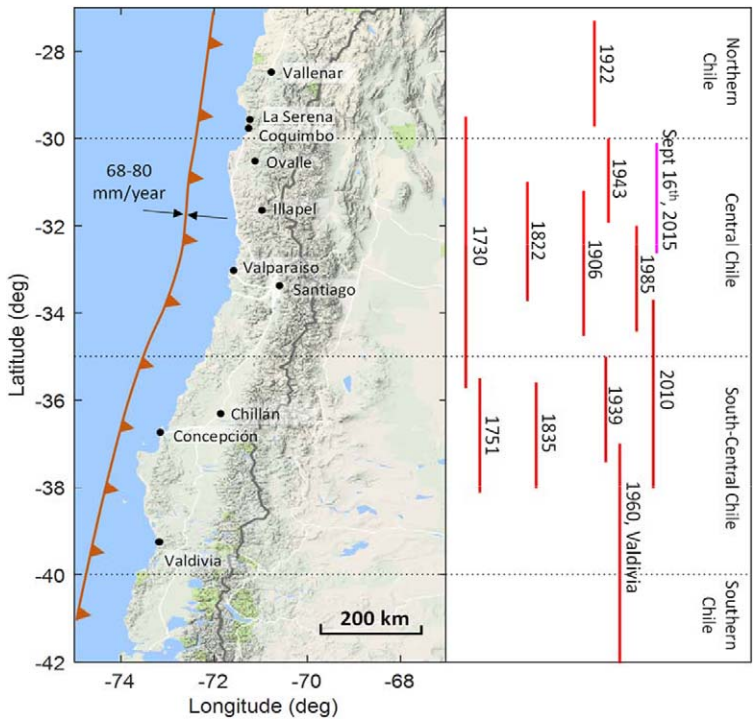

Figure 2. Estimated rupture lengths of the largest historical earthquakes in Central Chile since 1730 (modified after Dura et al. 2015).

settlement in bridge abutments were along Route 5 and interior roads. This article summarizes the main geotechnical aspects of the 16 September 2015 earthquake sequence and tsunami.

SEISMOLOGICAL BACKGROUND AND STRONG GROUND MOTIONS

The event was recorded by 44 ground motion stations and 15 GPS stations operated by the National Seismological Center (CSN - http://www.sismologia.cl). The Coquimbo Region experienced sparse seismicity in the months prior to September 16, with only 27 events of magnitude greater or equal than 4.5, as shown in Figure 3a. On the other hand, an important aftershock sequence followed the main event, with 361 earthquakes of magnitude $M_w \geq 4.5$, and 18 events with magnitude $M_w \geq 6.0$. Figure 3b presents the seismicity reported in the two months following the main event. The largest aftershocks took place 5 and 25 minutes after the main event, with magnitudes M_w 7.1 and 7.6, respectively.

Several finite fault solutions are available for this event (e.g., Heidarzadeh et al. 2016, Tilmann et al. 2016). For instance, NEIC (2015) estimated a maximum slip on the rupture plane that exceeds seven meters, and CSN determined that residual displacements concentrated on a 250 km stretch between latitudes 29.5°S and 32°S.

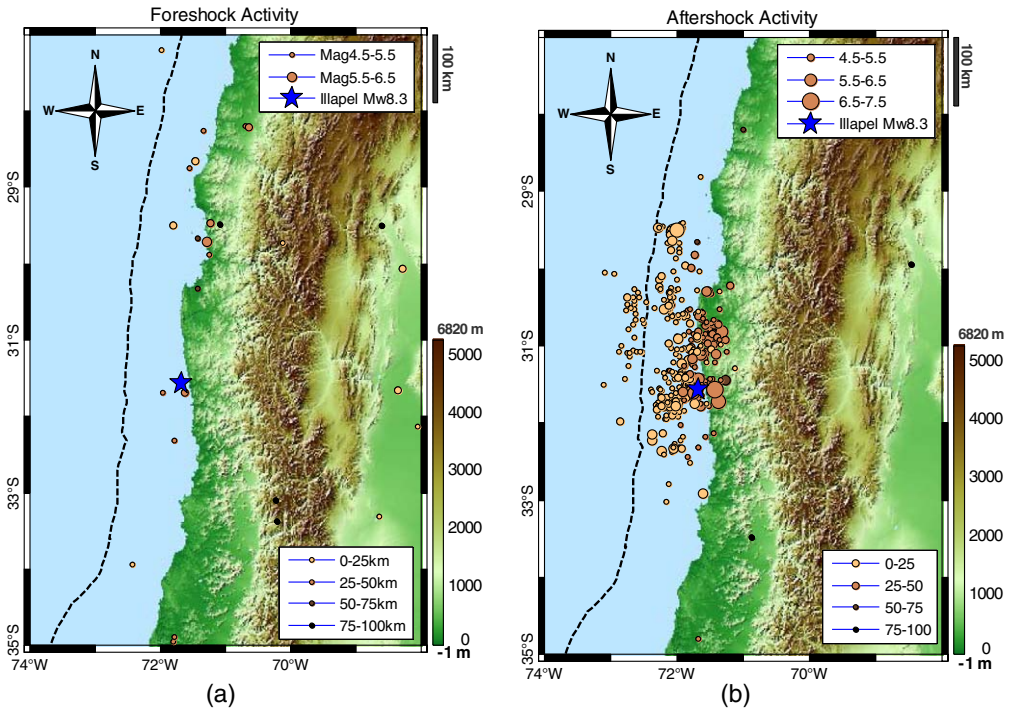

Figure 3. Topographic maps showing (a) the local seismicity 6 months before the main event, and (b) 2 months after. The circle color indicates the focal depth (km); the circle size indicates the magnitude according to the scale on the top right corner.

GROUND MOTION RECORDS

The available acceleration records correspond to 44 three-component ground motion (GM) stations plus 15 high-frequency GPS measurements with bandwidth from zero to 1 Hz. For the stations metadata and details about the record processing, the reader is referred to Bastías and Montalva (2016). Figure 4 presents the 5%-damped pseudo acceleration (*Sa*) spectra of the north-south and east-west components of the eight stations with highest peak ground acceleration (PGA).

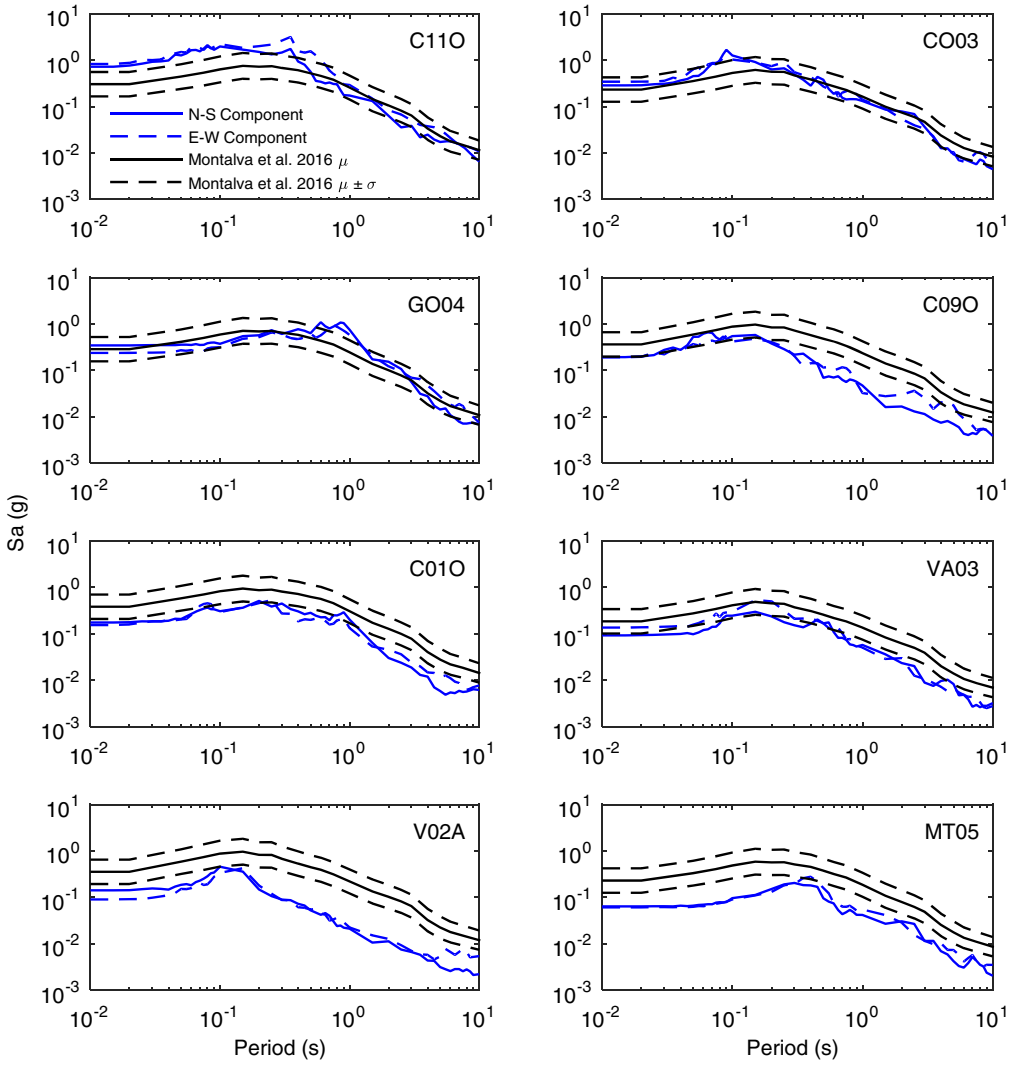

Figure 4. Spectral acceleration for the north-south and east-west components at eight recording stations compared against Montalva et al. (2016) estimates.

The acceleration spectra of Figure 4 shows that the recorded ground motion intensities are below the estimates by ground motion prediction equations (GMPE) suited for Chile (e.g., Montalva et al. 2016), especially in the high-frequency range. Most of the observed ground motions had lower *Sa* values than the expected for an M_w 8.3 event. Nevertheless, at station C11O, we observe *Sa* values in excess of the median plus one standard deviation for periods below 0.4 s. Likewise, at stations CO03 and GO04, the observed Sa is higher than the Montalva et al. (2016) estimates for periods around 0.1 s and 1.0 s, respectively, which indicates that these stations were perhaps affected by local site amplification.

The observed attenuation relation between *Sa* values and distance to the rupture plane is shown in Figure 5 for the 44 GM stations. Estimates of mean *Sa* values and mean plus/minus one standard deviation based on the event-corrected Montalva et al. (2016) model are also provided. Notice that in general, the observed Sa values are in good agreement with the GMPE estimates, which validates the use of this model to estimate ground motion intensities at sites where no ground motion records are available.

EXPECTED INTENSITIES AT NON-RECORDING SITES

The abovementioned GMPE developed by Montalva et al. (2016) is a frequency dependent model for 5%-damped pseudo-acceleration (*Sa*) suited for Chilean subduction earthquakes.

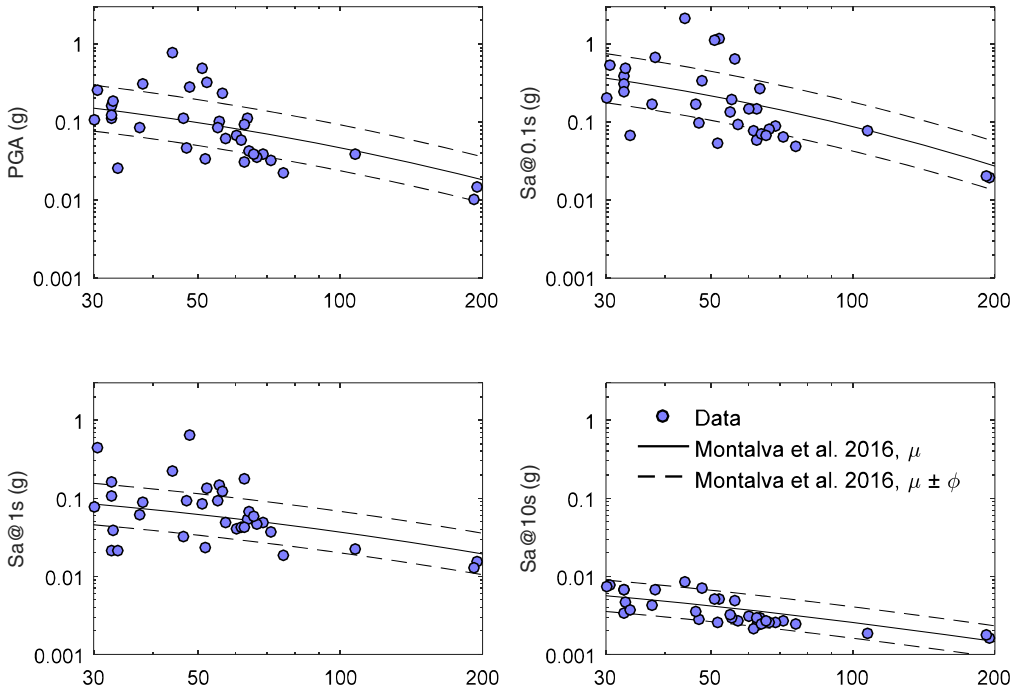

Figure 5. Measured 5% damped Sa attenuation with distance, and event-correct estimates based on Montalva et al. (2016).

This model follows the general form of modern GMPEs given by:

$$\ln(y) = \mu + \delta_{B_e} + \delta_{S2S} + \delta_{W_0} \tag{1}$$

where $\ln(y)$ represents the natural logarithm of the ground motion intensity, μ in the median model, and the residuals terms (i.e., δ_{B_e} event residual, δ_{S2S} site-to-site residual, and δ_{W_0} site remaining residual) allow to estimate the uncertainties associated with different components of the phenomena.

The median model is defined in terms of independent variables (e.g., M_w, R_{rup}, V_{S30}) and follows the Abrahamson et al. (2016) functional form. All the terms of Equation 1 were fitted using more than 3,000 records of processed Chilean ground motions. For more details on the ground motion model, the reader is referred to Montalva et al. (2016).

The best way to estimate ground motion intensities for this event at non-recording sites is using the known components of Equation 1. This implies that the best estimate, or event-corrected estimate, for a given site where no strong motion records are available is the mean plus the event residual, with the remaining residuals set equal to zero as shown in Equation 2:

$$\ln(y) = \mu + \delta_{B_e} \tag{2}$$

The event residuals in natural log units are -0.88 for PGA, then decrease to -0.97 close to $T = 0.1$ sec, to then increase up to -0.67 s at 10 s. The error in computing these event terms can be calculated performing a bootstrap analysis with available data, for further details the reader is referred to Montalva et al. (2016). Figure 6 shows the value of the event term for different periods along with its standard deviation. According to Equations 1 and 2, the negative residuals imply that the recorded intensities are lower than expected for an event with this event's magnitude, distance, and site conditions. The event-corrected model was used to estimate PGA for the liquefaction sites and the bridge abutments reported in the following sections.

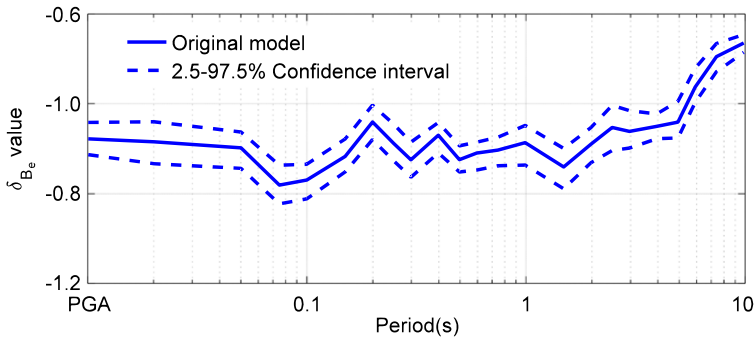

Figure 6. Event terms versus period along with its standard deviation for the Illapel earthquake.

EARTHQUAKE RECONNAISSANCE

The following section summarizes the main observations performed during the reconnaissance, and are organized in three sections (1) ground failure, (2) slope stability and rockfall, and (3) tsunami induced damage.

GROUND FAILURE

Retaining Structures

The overall performance of earth retaining structures in the region was satisfactory. Except for one failure, no significant damage was observed on gravity walls and other retaining structures supporting non-liquefiable backfills. Likewise, no evidence of seismically induced earth pressure damage was observed on MSE walls or building basements. Temporary support of excavations also performed well. For instance, in Coquimbo, a ~10 m deep excavation supported on soldier piles and anchors was flooded by the tsunami waves as shown in Figure 7a; however, the ground shaking caused no apparent damage on the retaining system.

A 30 m long section of a 4.5 m high gravity wall adjacent to Coquimbo's port failed by complete overturning, as shown in Figure 7b. The exposed backfill material was a mixture of very angular rock fragments (average size of 15 cm) and coarse beach sand. The measured peak horizontal and vertical accelerations at the nearest station are 0.25 g and 0.18 g respectively, peak ground velocity of 19 cm/s (located 1.9 km south of the site) and significant duration of 59 s; this level of acceleration is generally not sufficient to mobilize the shear strength of the retained material (Geraili Mikola et al. 2016), and thus, the likely cause of failure is the combined effect of hydrodynamic forces induced by the repeated tsunami waves and the ground shaking. Similar patterns of damage to quay walls and breakwaters

Figure 7. (a) Flooded excavation in Coquimbo (29.958°S, 71.338°W). No damage observed on the soldier piles and anchors; (b) failure of gravity walls at Coquimbo's waterfront (29.951°S, 71.336°W).

were observed in the Chile earthquake of 2010 (Bray and Frost 2010), and the Japan earthquakes of 1993 (Burcharth et al. 2001) and 2011 (Meneses and Arduino 2011).

Quay walls on Coquimbo's port were not damaged. Although access to the port facilities (run by a private company) was denied to the reconnaissance team, any observed damage was mostly due to flooding; no tilting was apparent on lamp posts or cranes, and no evidence of lateral spreading was observed in the corridors adjacent to the quay walls. Other similar retaining structures in the area survived the earthquake without damage.

Bridge Abutments

The Chilean Ministry of Public Works reported 8 bridges damaged on the Region of Coquimbo, which represent approximately 6.5% of the bridges in the region (MOP 2016). The most common damage patterns were the settlement of the bridge abutments and minor lateral spreading. Other less frequent effects were the damage of the bridge joints and excessive lateral displacement of concrete girders. Four of these bridges were surveyed by the reconnaissance team: El Teniente Bridge, Amolanas Bridge, La Cebada Bridge, and Illapel No. 2 Bridge.

El Teniente Bridge, located on the Quaternary marine terraces adjacent to Teniente Bay, is a five span reinforced concrete (RC) structure consisting of two spans 38.5 m long, and three spans 39.5 m long. The superstructure is made of a 0.2 m thick concrete slab and seven prestressed girders simply supported on neoprene bearing pads, a structural configuration commonly used in Chilean bridges (Moroni et al. 2008). The end abutments and the four intermediate piers are supported on ten piles 18 m in length, and 1.5 m in diameter. The ground motion caused a settlement in the south abutment of ~30 cm and a horizontal displacement of ~7 cm, leaving a residual deformation on the neoprene pads and large cracks in the approach pavement, as shown in Figure 8; the estimated PGA for rock is 0.25 g. Emergency ramps were built and the traffic flow was restored soon after.

A similar situation was observed in the Illapel No. 2 Bridge (31.631°S, 71.157°W), located in the Quaternary fluvial deposits of the Illapel River (Martínez 2003). The 150 m long bridge, a six-span steel girder structure, is underlain by a matrix of coarse gravels

Figure 8. (a) Concrete girders and piers of El Teniente bridge, (b) south approach before temporary repairs, (c) deformed neoprene bearings on the south abutment. (30.995°S, 71.631°W).

and clean sand. The ground motion at the site, with an estimated PGA of 0.18 g, caused a 10 cm settlement of the north and south abutments, and minor raveling of the abutment slopes. In both cases, no settlement was observed on the bridge piers.

Other bridges inspected showed only slight damage or no damage at all. For instance, the Amolanas Viaduct in Route 5, one of the tallest bridges in South America, underwent no structural or geotechnical damage. The viaduct has a total length of 268 m and four spans (40, 60, 80, and 88 m), Figure 9; the deck consists of a continuous steel box supported on three RC piers of height 22.3 m, 49.1 m and 95.6 m, and is equipped with friction isolators and viscous dampers. The foundations are supported on folded layers of sedimentary rocks, and sandstone conglomerate with excellent bearing capacity. The southern and northern slopes are reinforced with rock bolts (González Rodríguez 2008).

Sand boils were observed just north of El Teniente Bride in the river bed of La Cebada Bridge (30.973°S, 71.642°W), however, no settlement was observed in the bridge approach, only minor concrete spalling in the girders due to impact with the abutment walls. Overall, retaining structures and bridges performed well, and other than the collapsed gravity walls near Coquimbo's port, no significant damage or catastrophic failures were reported.

Liquefaction

When documenting the effects of major earthquakes, it is important to note areas both with and without impact on built structures to better understand the geotechnical and geologic factors that control co- and post-seismic ground deformations. Liquefaction during the 2015 Illapel main shock and aftershocks was not extensive, however, local damage was observed in structures including bridges, sewers lines, roads, power lines, and buildings. All sites were investigated both by road and on foot to document the occurrence (or lack thereof) of liquefaction. Field observations were supplemented by visual interpretation of aerial imagery using Google Earth. A combination of low-groundwater levels (due to semi-arid climate and persistent drought) combined with limited distribution of liquefaction-susceptible deposits in the area contributed to the limited distribution of observed liquefaction from the 2015 Illapel earthquake sequence.

In contrast to mass-wasting, which was widespread across the rupture area, liquefaction occurrence was much more localized and limited to areas with near-surface groundwater

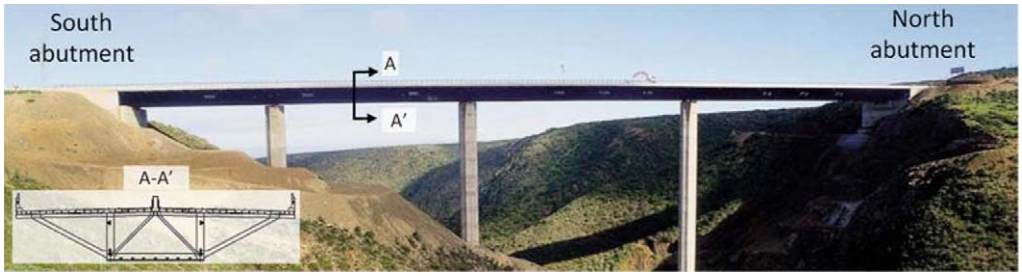

Figure 9. Amolanas Viaduct, no damage observed (31.174°S, 71.608°W).

(e.g., adjacent to the coast, lagoons, rivers and creeks) and suitable sediments for liquefaction susceptibility. No liquefaction was observed between Los Vilos and Tongoy; most evidence was found north of Tongoy and north to La Serena.

Six sites were documented and are discussed below. Importantly, five of these sites were visited post-earthquake with equipment for shear wave velocity characterization. Surface-wave based techniques were used to obtain Rayleigh wave dispersive properties at these sites. The shear wave velocity profiles were then estimated by solving an inverse problem and the neighborhood algorithm (Wathelet 2008). A combination of source-controlled (active) with ambient noise (passive) techniques was used, with sensors arranged in several arrays to capture different wavelengths. This approach was previously used by several authors (Tokimatsu 1997, Humire et al. 2015, Becerra 2015). Figure 10a shows the measured shear wave velocity profiles at the five sites, along with the Vs-based factors of safety against liquefaction according to the deterministic approach proposed by Kayen et al. (2013). For this purpose, a moment magnitude of $M_w = 8.3$ was considered along with the PGA's estimated using Montalva et al. (2016): 0.160 g (Site 1), 0.161 g (Site 2), 0.161 g (Site 3), 0.162 g (Site 4), and 0.178 g (Site 5). Also, it was assumed that the groundwater table was located at the surface, that the soils had a uniform total density of $20\,\mathrm{kN/m^3}$, and that the fines content was below 5%. Soil layers with factors of safety below 1.5 were considered to be potentially liquefiable during the event; in Figure 10a they were drawn with filled markers to distinguish them from layers that likely did not liquefy (open markers).

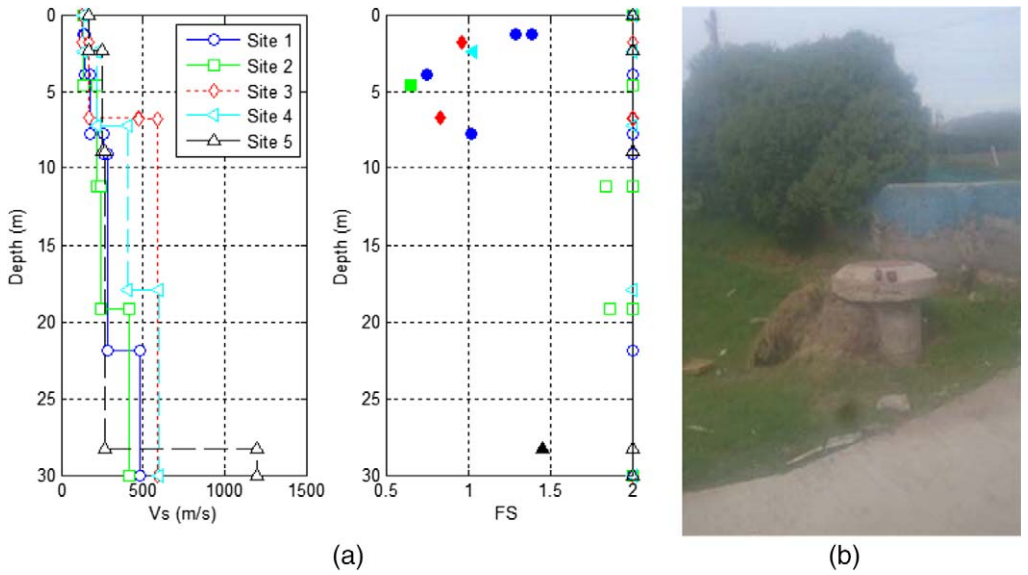

Figure 10. (a) Measured shear wave profiles and factors of safety from liquefaction triggering analysis, and (b) field photograph of Los Pescadores street sewer portal (Site 4) after a number of M_w 6+ aftershocks (29.951°S, 71.295°W).

Liquefaction Site 1 – Santa Margarita Del Mar Building Complex (29.896°S, 71.268°W)

At the Santa Margarita del Mar building complex, no evidence of liquefaction was observed during the week of October 5, 2015, although the liquefaction susceptibility analysis shows that liquefaction could have taken place at depths between ~4 m and ~8 m in rather thin layers.

Liquefaction Site 2 – La Serena Lighthouse (El Faro) (29.905°S, 71.274°W)

This is a site where no evidence of liquefaction and lateral spreading was found and, if it occurred, the surface evidence was likely altered by tsunami waves, which also caused scour here. The site subsided and the V_S-based liquefaction susceptibility analysis indicated that the critical layer was at a depth of 4.5 m. Cracks from previous damage to El Faro (damage occurred sometime between 1953 and 2015), were filled with concrete and painted over and then re-opened, due to renewed subsidence during the Illapel earthquakes. CPT investigations here in the future will further assist with the liquefaction susceptibility at this location to allow a better characterization between damage due to foundation scour and from liquefaction during strong ground motions.

Liquefaction Site 3 – Main N-S Road Along the Coast South of the Casino between La Serena and Coquimbo (29.954°S, 71.302°W)

This is also a site altered by the tsunami waves, and thus, no surface evidence of liquefaction and lateral spreading was observed. The liquefaction susceptibility analysis shows that liquefaction could have taken place at depths of ~2 m and ~6.5 m. Subtle circular sand blows (~1 m diameter) were observed at this site, similar to liquefaction sand boils observed in the 2010 Darfield earthquake (Green et al. 2010). The tsunami waves that overtopped the coastal road washed away any traces of ejecta or other evidence of liquefaction.

Liquefaction Site 4 – Near Coast in La Serena with Lateral Spreading and Sewer Pipes Uplift (29.951°S, 71.295°W)

This site exhibited clear evidence of liquefaction and lateral spreading of a ~600 m long strip parallel to the coast in La Serena. Here, deformation was evident with liquefaction and lateral-spreading-induced floating of concrete sewer services (i.e., flotation, raised sewer portals and raised pipes), vertical subsidence noted with cracked ground, normal (downward) faulted blocks of soil, cracks within nearby roads and tilted power poles (Figure 10b). The V_S-based liquefaction susceptibility analysis indicated that the critical layer was at a depth of 2.5 m. The first observations here were taken one week after the earthquake. The sites were revisited one week later (week of October 5, 2015) at which time they showed continued deformation (i.e., subsidence, likely due to numerous $M_w > 6$ aftershocks during this one-week period).

Liquefaction Site 5 – Old Bridge on Route D-420 Near Tongoy (30.261°S, 71.481°W)

The old Tongoy Bridge of route D-420 is a two lane RC bridge built in the 1960s located in the north access of Tongoy Bay. This bridge was closed permanently on 2012 due to lack of maintenance and a significant settlement in the north abutment. After the 2015 earthquakes, the north abutment continued deforming and accumulated a settlement of over 1.5 m, as shown in Figure 11. The V_S-based susceptibility analysis did not predict liquefaction at this site.

Figure 11. Field photograph looking south of the D-420 bridge. Northern end of the bridge has a vertical step where it failed during the earthquake. People shown for scale (30.261°S, 71.481°W).

Geologic profiles in the Tongoy Bay (Meinardus 1961) show that the area is underlain by unconsolidated layers of gravel, sandy clay of fluvial origin, along with marine sands and clay.

Liquefaction Site 6 – Edificios La Serena (29.949°S, 71.282°W)

Based on pre-earthquake site investigation data (Ruz 2015, *pers. comm.*), liquefaction was expected at this site. However, no signs of liquefaction were observed (based on visit on October 9). This could have been because the entire site was pre-excavated up to 4 m to 5 m deep and replaced with engineered fill, and likely reduced liquefaction susceptibility in the upper 4–5 m.

SLOPE STABILITY AND ROCKFALLS

Mass-wasting was widespread along roads and cut slopes within the zone of deformation of the earthquake rupture, leading to total or partial blockage on several roads (with some being important "lifelines"). No deep-seated landslides were observed; although over such a large area, some are perhaps in locations that were not covered by the reconnaissance. This investigation focused on rockfalls estimated to be at least 3 m^3 in volume, along important lifelines such as the Route 5 (Pan-American Highway), and inland roads along the transverse valleys.

Route 5 (The Pan-American Highway) runs north-south parallel to the coast. The highway is divided into two, two-lane northbound and southbound routes through hilly to mountainous terrain. To bring Route 5 to grade during construction, a number of cut slopes in both rock and sediment were developed leaving over-steepened faces adjacent to the highway. A number of these slopes were engineered to stop rockfall (e.g., fencing), however in a number of cases the volume of mass-wasting caused the mitigation strategies to fail. Mass-wasting covered Route 5 in sections, blocking the entire northbound or southbound lanes, as shown in Figure 12; however, to our knowledge, no single rockfall covered both lanes in both directions.

North of La Serena and outside of the main zone of deformation (e.g., outside of the zone of slip during the events), slopes were not impacted as greatly as south of La Serena.

Figure 12. Rockfalls on Route 5: (a) northbound lane at km 334 (31.004°S, 71.624°W), mitigation fences were destroyed, both lanes were closed after the earthquake and one lane remained closed for at least 10 days; and (b) southbound lane at km 280 (31.444°S, 71.564°W), one lane was blocked following the earthquake.

Likewise, near La Higuera (~50 km north of La Serena) no slope stability issues were noted, except for one sedimentary road cut before Honda Pass (29.609°S, 71.258°W), where Route 5 climbs ~600 m above sea level with a number of major cut slopes. This demonstrates a correlation between the location of slip during the earthquakes and slope stability distribution (i.e., observed geotechnical effects were limited to the north and south of the zone of tectonic deformation). This suggests that the rupture area in major megathrust events controls the areas where rockfall impacts in future events will be greatest.

Numerous topples or slumps were observed in over-steepened road cuts through weathered igneous rocks and sediments, even where fences or other mitigation measures were in place. Oftentimes, these over-steepened cut slopes had estimated inclinations of 4:1 (V:H) or steeper, and estimated heights between 5 m to 30 m. In some locations, rockfall occurred along bedding planes, however most rockfall occurred from cliffs composed of highly fractured (i.e., jointed) and weathered igneous rocks, which failed due to strong ground motion. No rockfall or slope stability issues were noted along the flatter sections along Route 5.

In addition to Route 5, several inland roads in the region were visited, including asphalted routes D-55, D-71, D-81, D-85, and dirt Routes D-75 and D-951 which run along the Choapa River. These roads cross hilly terrain and the east-west fluvial transverse valleys in the region. In some areas these roads run parallel to nearly vertical cliffs, and the earthquakes caused widespread damage to steep cut-slopes of sedimentary rocks and weathered igneous rocks, temporarily blocking traffic on one or two lanes, as shown in Figure 13.

One week after the main shock, most asphalted roads had been cleared off and the traffic was fully restored; only a few rural roads remained blocked due to large rockfall.

Figure 13. Traffic discontinued on Route D-75 as a result of rockfalls. Estimated volume > 200 m^3 (31.5855°S, 71.4674°W).

Several sections of Route D-85 were previously reinforced with wire meshes and parapets to prevent rockfall from blocking the road. In general, these systems performed well as they caught the loose soil and small blocks of fractured rock, in some locations however the wire mesh was completely destroyed and the parapets overtopped.

Importantly, by comparing the distribution of slip within the event as revealed by seismic and GPS studies (Tilmann et al. 2016), with our distribution of rockfall/mass-wasting (Figure 14), zones within the coseismic deformation zone, experienced the most amount of rockfall. This suggests that in future earthquakes, a model of coseismic tectonic slip (which can be generated rapidly post-earthquake) may provide insight important into where the most amount of rockfall or landslides will be located and where resources should be devoted to keep lifelines open.

A large boulder of size 3–4 m^3 fell off the hillslope and destroyed a house in Puerto Oscuro (31.422°S, 71.595°W), and there are likely a number of "one-off" rockfalls that occurred within the rupture area. While the fall of single boulders from natural or engineered slopes was common, the effect on the infrastructure was generally limited.

TSUNAMI-INDUCED DAMAGE

Tsunami waves struck the coast of the rupture region following the Illapel earthquake. The tsunami effects were observed over at least 350 km along the coast from Valparaiso to La Serena. A range of tsunami heights were measured using a barometric altimeter calibrated at the moment of each observation and then corrected by tide effects based on information from the Chilean Navy Hydrographic and Oceanographic Service (SHOA 2015), yielding an error of ±0.5 m. The highest pervasive marks left by razed vegetation were recorded, but also traces of erosion and scour on the beach, and sand and boulder deposits. Two areas of maximum run-up height (e.g., the maximum elevation above sea level) were observed associated to the two main rupture patches, one reaching 5–6 m near Los Vilos just

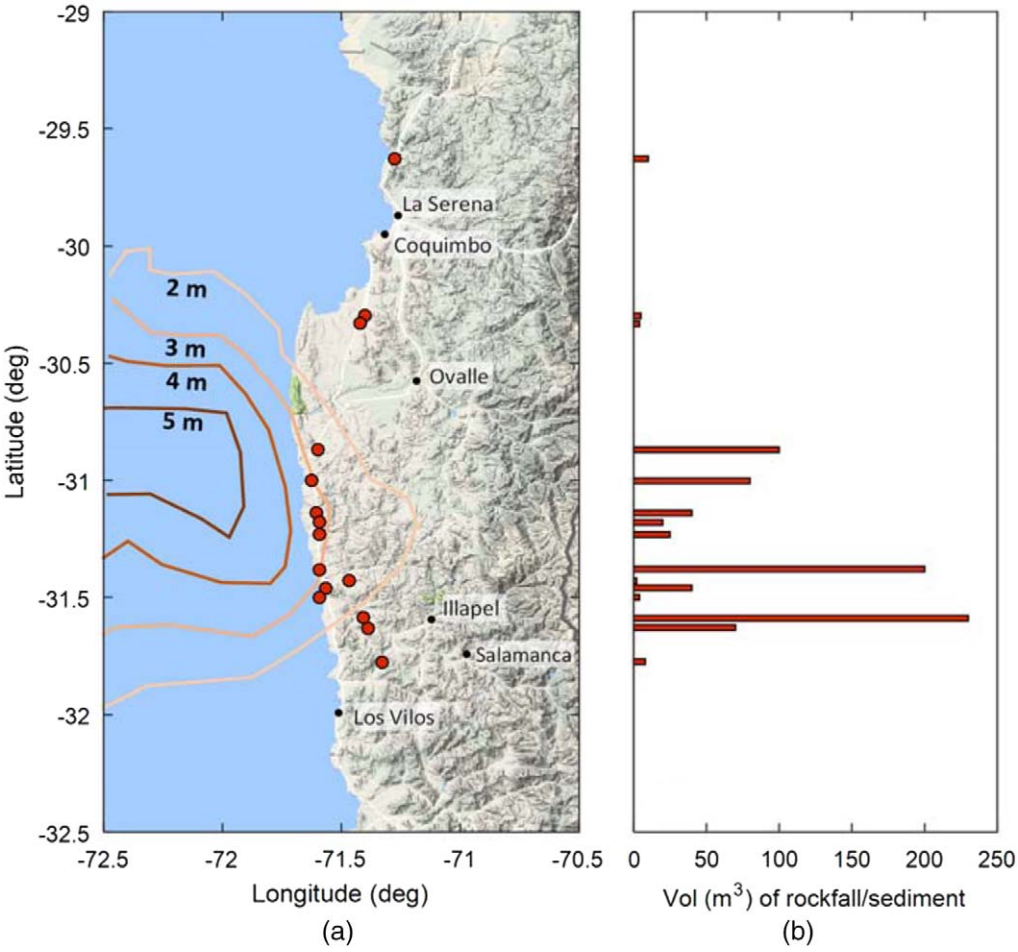

Figure 14. (a) Map showing some key rockfall locals along Route 5 (red dots) with a coseismic slip model (in m), after Tilmann et al. 2016. (b) Rockfall volumes (m^3) versus latitude observed along the Route 5. Note the striking correspondence between the slip and observed rockfall, which suggests that rockfall is greatest and concentrated in the locations where the most tectonic slip occurred.

south of the epicenter (31.912°S, 71.513°W), and the other reaching 10–11 m north of the epicenter in the fishing town Totoral (30.365°S, 71.667°W) (Aránguiz 2016). According to witnesses, the first tsunami wave reached the coastline nearest to the epicenter no more than 5–7 minutes after the main shock. In the City of Coquimbo, the first arrival was measured 23 min after the main shock; and within the next two hours was followed by three waves of height between 4–5 m and several smaller waves (Aránguiz 2016). A tsunami alert message was issued 8 minutes after the main event and the entire Chilean coast was ordered to evacuate, which combined with ongoing earthquake and tsunami education helped to significantly reduce the number of casualties (estimated to be eight people) in comparison of previous destructive tsunamis (Lomnitz 1970, Fritz et al. 2011).

Figure 15. (a) Sand and rock fills in Coquimbo's shoreline washed away by tsunami waves (29.956°S, 71.336°W), and (b) tsunami erosion and scour along Avenida Costanera, Coquimbo (29.961°S, 71.328°W).

Tsunami waves caused severe damage to Coquimbo's waterfront. The measured inundation depth in the bay was over 4.5 m and extended over a distance of ~500 m from the coast in some areas (GEER 2015). As a result, several lightweight structures were washed away, lifelines were interrupted, and the inundation zone was left with several tons of tsunami debris (including fishing boats that were carried onshore). Along Avenida Costanera (Coquimbo's coastline road), several residential buildings were flooded, and the sand and rock fill along the road were heavily eroded and occasionally washed away by the tsunami waves (Figure 15).

The tsunami waves inundated a number of areas further afield from the coast as could be seen with debris lines on fences and other structures up to 200 m away from the shoreline. Similar effects were observed in small fishing towns in the coast near the epicenter, like Huentelauquén, Caleta Sierra (El Maitén), Caleta el Sauce, Caleta Talcacura, and Caleta El Totoral. At Caleta Sierra, for instance, tsunami waves reached an inundation depth of ~4 m, strongly impacting the lower area of the embayment and causing destruction of several houses and fishing boats. In the southern end of the rupture area, near Los Vilos, a number of houses adjacent to the beach were completely destroyed or damaged beyond repair. Sand from these waves was carried inland and likely obscured liquefaction evidence during erosion and deposition after the tsunami waves receded.

CLOSING REMARKS

Subduction-zone earthquakes present particular challenges to the built environment along coasts. The strong ground motions during 16 September 2015 caused minor to moderate damage to the built infrastructure in the Coquimbo Region, in part due to Chile's strong building codes. The tsunami waves generated during this earthquake however, caused severe damaged to vital infrastructure in the cities of Coquimbo, Los Vilos, and Tongoy, and

anticipation of these waves triggered a massive evacuation of the coast. The reconnaissance team documented evidence of the geotechnical effects of the earthquake, including spread erosion and scouring in the borderline, liquefaction of loose sands deposits, settlement in bridge abutments, the response of gravity retaining structures, and several cases of rockfalls in steep road cuts. Documenting these observations is key for appraising the regional impact of such extreme natural disasters and provides an empirical base for improving seismic risk decision making. Importantly, engineers and geologists documenting post-earthquake effects should be careful to not exclude the effects of tsunami waves concealing perishable evidence of ground failure or other types of co- and post-seismic effects that impact the infrastructure. Specifically, it is important to understand the effects of tsunami waves, which redistributes enormous amounts coastal and nearshore sediments (oftentimes sand) which oftentimes erase any trace of liquefaction at the surface. Additionally, the zones that experienced the greatest coseismic slip (e.g., Tilmann et al. 2016, Figure 14), appeared to have the largest volumes of rockfall that impacted roads, which suggests that coseismic slip maps generated immediately post-earthquake (generated from seismic records and GPS data) can provide a first order indication about where to expect damage to infrastructure during future events due to slope stability issues. Likewise, the evidence gathered and reported herein should be helpful when conducting in depth studies associated to the behavior of specific aspects of this event.

ACKNOWLEDGMENTS

The authors greatly appreciate the support of the Geotechnical Extreme Events Reconnaissance (GEER) Steering Committee, in particular Prof. Jonathan Bray for supporting this research. Funding for this work was provided by the National Research Center for Integrated Natural Disaster Management CONICYT/FONDAP/ 15110017; Candia was also sponsored by Universidad del Desarrollo. De Pascale and the Universidad de Chile group were supported by a FCFM (UChile) academic fund and CEGA FONDAP CONICYT 15090013. Montalva and the Universidad de Concepción group were funded by FONDECYT 1140317 and Water Research Center for Agriculture and Mining CONICYT/FONDAP/15130015. Ledezma was funded by FONDECYT 11110125 and by CONICYT USA2012-0007. Thanks to Prof. Gabriel Vargas for providing some Tsunami observations. Thanks to Prof. Esteban Sáez and his team for performing the shear wave velocity measurements. Participation of GEER Steering Committee personnel in coordinating and reviewing the report was made possible by the U.S. National Science Foundation (NSF) through Grant No. CMMI-1266418. Any opinions, findings, and conclusions or recommendations expressed in this material are those of the authors and do not necessarily reflect the views of the NSF.

REFERENCES

Abrahamson, N. A., Gregor, N., and Addo, K., 2016. BC Hydro ground motion prediction equations for subduction earthquakes, *Earthquake Spectra* **32**, 23–44.

Aránguiz, R., González, G., González, J., Catalán, P. A., Cienfuegos, R., Yagi, Y., Okuwaki, R., Urra, L., Contreras, K., Del Rio, I., and Rojas, C., 2016. The 16 September 2015 Chile tsunami from the post-tsunami survey and numerical modeling perspectives, *Pure and Applied Geophysics* **173**, 333–348.

Bastías, N., and Montalva, G. A., 2016. Chile strong ground motion flatfile, *Earthquake Spectra* **32**, 2549–2566.

Burcharth, H. F., Bernal, A., Blazquez, R., Dickenson, S. E., Ferritto, J., Finn, W. L., Iai, S., Ichii, K., Mccullough, N. J., Meeuwissen, P. W. H., Memos, C. D., Priestley, M. J. N., Silvestri, F., Simonelli, A. L., Steedman, R. S., and Sugano, T., 2001. Seismic design guidelines for port structures, available at http://philpapers.org/rec/BURSDG.

Becerra, A., 2015. Seismic Microzoning of Arica and Iquique, Chile, M.S. Thesis, Pontificia Universidad Católica de Chile.

Bray, J., and Frost, D., 2010. *Geo-Engineering Reconnaissance of the 2010 Maule, Chile Earthquake*, Report No. GEER-022 of the NSF Sponsored GEER Association Team, 1.

Dura, T., Cisternas, M., Horton, B. P., Ely, L. L., Nelson, A. R., Wesson, R. L, and Pilarczyk, J. E., 2015. Coastal evidence for Holocene subduction-zone earthquakes and tsunamis in central Chile, *Quaternary Science Reviews* **113**, 93–111.

Fritz, H. M., Petroff, C. M., Catalán, P. A., Cienfuegos, R., Winckler, P., Kalligeris, N., Weiss, R., Barrientos, S. E., Meneses, G., Valderas-Bermejo, C., Ebeling, C., Papadopoulos, A., Contreras, M., Almar, R., Dominguez, J. C., and Synolakis, C. E., 2011. Field survey of the 27 February 2010 Chile tsunami, *Pure and Applied Geophysics* **168**, 1989–2010.

Geotechnical Extreme Events Reconnaissance Association (GEER), 2015. *Geotechnical Reconnaissance of the 2015 M_w 8.3 Illapel, Chile Earthquake*, Report No. GEER-043, Version 1, available at DOI:10.18118/G6QG66.

Green, R. A., Cubrinovski, M., Allen, J., Ashford, S., Bowman, E., Bradley, B. A., Cox, B., Cubrinovski, M., Green, R. A., Hutchinson, T., Kavazanjian, E., Orense, R., Pender, M., Quigley, M., and Wotherspoon, L., 2010. *Geotechnical Reconnaissance of the 2010 Darfield (New Zealand) Earthquake*, GEER Report, available at DOI:10.18118/G6D59F.

Geraili Mikola, R., Candia, G., and Sitar, N., 2016. Seismic earth pressures on retaining structures and basement walls in cohesionless soils, *Journal of Geotechnical and Geoenvironmental Engineering*, 04016047.

González Rodríguez, G., 2008. Análisis No-Lineal del Puente Amolanas Usando Registros Sísmicos de Aceleración y Desplazamiento, available at http://www.repositorio.uchile.cl/handle/2250/103104.

Heidarzadeh, M., Murotani, S., Satake, K., Ishibe, T., and Gusman, A. R. (2016), Source model of the 16 September 2015 Illapel, Chile, M_w 8.4 earthquake based on teleseismic and tsunami data, Geophys. Res. Lett., **43**, 643–650, DOI: 10.1002/2015GL067297.

Humire, F., Sáez, E., Leyton, F., and Yáñez, G., 2015. Combining active and passive multi-channel analysis of surface waves to improve reliability of V_{S30} estimation using standard equipment, *Bull Earthq Eng* **13**, 1303–1321.

Kayen, R., Moss, R. E. S., Thompson, E. M., Seed, R. B., Cetin, K. O., Kiureghian, A. D., Tanaka, Y., and Tokimatsu, K., 2013. Shear-wave velocity–based probabilistic and deterministic assessment of seismic soil liquefaction potential, *Journal of Geotechnical and Geoenvironmental Engineering* **139**, 407–419.

Lomnitz, C., 1970. Major earthquakes and tsunamis in Chile during the period 1535 to 1955, *Int. J. Earth Sci.* **59**, 938e960.

Martínez, C., Rebolledo, S., Espinoza, C., and Parraguez, C., 2003. Caracterización del Relleno de la Cuenca del Río Illapel, entre Huintil y el Peral, in *Actas X Congreso Geológico Chileno*, Universidad de Concepción, Chile, available at http://biblioteca.sernageomin.cl/opac/DataFiles/MartinezC_et_al.pdf (in Spanish).

Meinardus, H., 1961. Exploraciones geofísicas en el área de Tongoy, Editorial Universitaria, available at http://www.revistas.uchile.cl/index.php/AFCFM/article/download/37158/38731.

Meneses, J., and Arduino, P., 2011. *Preliminary Observations of the Effects of Ground Failure and Tsunami on the Major Ports of Ibaraki Prefecture*, GEER Assoc. Rep. No. GEER-025c.

Montalva, G., Bastías, N., and Rodriguez-Marek, A., 2016. Ground Motion Prediction Model for the Chilean subduction zone, *Bulletin of the Seismological Society of America*, in press.

Moroni, O., Sarrazin, M., Benavides, C., and Díaz, A., 2008. Características dinámicas de puentes Chilenos con protección sísmica, *Revista Sul-americana de Engenharia Estrutural* **1**.

National Earthquake Information Center (NEIC), 2015. Earthquake data web page for the 16 September 2015 magnitude 8.3 - 48km W of Illapel, Chile, available at http://earthquake.usgs.gov/earthquakes/eventpage/ us20003k7a#scientific_finite-fault (last accessed 4 March 2016).

MOP, 2016. Observatorio de la Infraestructura y Gestión del recurso Hídrico, available at http://www.dirplan.cl/centrodedocumentacion/Documents/SIT%20MOP/Mapas/PUENTES_SHP.zip.

Servicio Hidrográfico y Oceanográfico de la Armada (SHOA), n.d. www.shoa.cl. (last accessed on 10 November 2015).

Tilmann, F., et al. 2016. The 2015 Illapel earthquake, central Chile: A type case for a characteristic earthquake?, *Geophys. Res. Lett.* **43**, 574–583, DOI:10.1002/2015GL066963.

Tokimatsu, K., 1997. Geotechnical site characterization using surface waves, in *Proceedings of the 1st International Conference on Earthquake Geotechnical Engineering* **3**, 1333–1368.

U.S. Geological Survey (USGS), 2016. Earthquake Hazard Program M8.3-48 km W of Illapel, Chile ShakeMap, available at http://earthquake.usgs.gov/earthquakes/eventpage/us20003k7a#shakemap (last accessed 28 July 2016).

Wathelet, M., 2008. An improved neighborhood algorithm: parameter conditions and dynamic scaling, *Geophys Res Lett* **35**, L09301.

(Received 17 March 2016; accepted 15 January 2017)